NAVAL POSTGRADUATE SCHOOL

MONTEREY, CALIFORNIA

THESIS

NAVAL ELECTRIC WEAPONS: THE ELECTROMAGNETIC RAILGUN AND FREE ELECTRON LASER

by

Robert E. Williams

June 2004

Thesis Advisor: William B. Colson
Second Reader: Robert L. Armstead

Approved for public release; distribution is unlimited

THIS PAGE INTENTIONALLY LEFT BLANK

REPORT DOCUMENTATION PAGE

Form Approved OMB No. 0704-0188

Public reporting burden for this collection of information is estimated to average 1 hour per response, including the time for reviewing instruction, searching existing data sources, gathering and maintaining the data needed, and completing and reviewing the collection of information. Send comments regarding this burden estimate or any other aspect of this collection of information, including suggestions for reducing this burden, to Washington headquarters Services, Directorate for Information Operations and Reports, 1215 Jefferson Davis Highway, Suite 1204, Arlington, VA 22202-4302, and to the Office of Management and Budget, Paperwork Reduction Project (0704-0188) Washington DC 20503.

1. AGENCY USE ONLY (*Leave blank*)	2. REPORT DATE June 2004	3. REPORT TYPE AND DATES COVERED Master's Thesis	
4. TITLE AND SUBTITLE: Naval Electric Weapons: The Electromagnetic Railgun and Free Electron Laser		**5. FUNDING NUMBERS**	
6. AUTHOR Robert E. Williams			
7. PERFORMING ORGANIZATION NAME(S) AND ADDRESS(ES) Naval Postgraduate School Monterey, CA 93943-5000		**8. PERFORMING ORGANIZATION REPORT NUMBER**	
9. SPONSORING /MONITORING AGENCY NAME(S) AND ADDRESS(ES) N/A		**10. SPONSORING/MONITORING AGENCY REPORT NUMBER**	

11. SUPPLEMENTARY NOTES The views expressed in this thesis are those of the author and do not reflect the official policy or position of the Department of Defense or the U.S. Government.

12a. DISTRIBUTION / AVAILABILITY STATEMENT Approved for public release; distribution is unlimited	12b. DISTRIBUTION CODE A

13. ABSTRACT (maximum 200 words)

Theory and simulations of the railgun and free electron laser are presented, as well as a suggestion for extending the railgun lifecycle. The theory, design, and analysis of an electromagnetic railgun using a numerical model are discussed. The effects of varying electrical pulse formations, rail materials and geometries are explored. The application of a metallurgical process to mitigate hypervelocity gouging in railgun rails is proposed. This concept, to delay the onset velocity of gouging by laser-peening rails surfaces, may significantly increase the velocity at which projectiles acceptably traverse the barrel and extend the useful life of rails. If successful, this process would apply to any pair of materials in sliding contact at high relative velocity, including rocket sled tracks and light gas guns barrels. The status of proof-of-concept tests at LLNL, UC Davis, and UT is covered. FEL simulations investigating the effect that electron beam focal point variations have on the optical mode within the undulator are presented.

14. SUBJECT TERMS **Free Electron Laser, Short Rayleigh Length, Directed Energy, Optical Mode, Railgun, Simulation, Gouging**			15. NUMBER OF PAGES 69
			16. PRICE CODE
17. SECURITY CLASSIFICATION OF REPORT Unclassified	18. SECURITY CLASSIFICATION OF THIS PAGE Unclassified	19. SECURITY CLASSIFICATION OF ABSTRACT Unclassified	20. LIMITATION OF ABSTRACT UL

THIS PAGE INTENTIONALLY LEFT BLANK

ELECTRIC WEAPONS: THE ELECTROMAGNETIC RAILGUN AND FREE ELECTRON LASER

Robert E. Williams
Lieutenant, United States Navy
B.S., Industrial Engineering, Auburn University, 1999

Submitted in partial fulfillment of the
requirements for the degree of

MASTER OF SCIENCE IN APPLIED PHYSICS

from the

**NAVAL POSTGRADUATE SCHOOL
June 2004**

Author: Robert E. Williams

Approved by: William B. Colson
                  Thesis Advisor

                  Robert L. Armstead
                  Second Reader/Co-Advisor

                  James H. Luscombe
                  Chairman, Department of Physics

THIS PAGE INTENTIONALLY LEFT BLANK

ABSTRACT

Theory and simulations of the railgun and free electron laser are presented, as well as a suggestion for extending the railgun lifecycle. The theory, design, and analysis of an electromagnetic railgun using a numerical model are discussed. The effects of varying electrical pulse formations, rail materials and geometries are explored. The application of a metallurgical process to mitigate hypervelocity gouging in railgun rails is proposed. This concept, to delay the onset velocity of gouging by laser-peening rails surfaces, may significantly increase the velocity at which projectiles acceptably traverse the barrel and extend the useful life of rails. If successful, this process would apply to any pair of materials in sliding contact at high relative velocity, including rocket sled tracks and light gas guns barrels. The status of proof-of-concept tests at LLNL, UC Davis, and UT is covered. FEL simulations investigating the effect that electron beam focal point variations have on the optical mode, gain, and extraction within the undulator are presented.

THIS PAGE INTENTIONALLY LEFT BLANK

TABLE OF CONTENTS

LIST OF FIGURES

THIS PAGE INTENTIONALLY LEFT BLANK

LIST OF TABLES

THIS PAGE INTENTIONALLY LEFT BLANK

LIST OF SYMBOLS

Throughout this thesis, mks units were used, except for the dimensionless variables mentioned below, which are defined in the text.

A area perpendicular to the magnetic field

A_{cs} cross-sectional area of rails

a acceleration

a_o dimensionless optical field strength

B magnitude of the railgun circuit magnetic field

$\dot{B}$ vector of the railgun circuit magnetic field

B_m magnitude of the undulator magnetic field

$\dot{B}_m$ vector of the undulator magnetic field

B_{rms} root-mean-square of the magnetic field strength

C capacitance

c speed of light

c_h specific heat

E electron energy

dE change in thermal energy

dt differential time

E_s optical electric field amplitude

e electron charge

F_L Lorentz force

$\dot{F}_L$ vector of the Lorentz force

$\dot{F}_{L1}$ vector of the Lorentz force for a single rail

G optical gain for a single pass

h height of rails

I railgun current

I_{ave} average electron beam current

I_{peak} peak electron beam current

j dimensionless electron current

K	dimensionless undulator parameter
k	optical wave number
k_o	undulator wavenumber
L	electrical inductance
L'	inductance gradient
L_r'	inductance gradient of the rails
L_c	circuit inductance
L_r	rail inductance
L_u	undulator length
l	length in the direction of current
l_b	micropulse length
m	projectile mass
m_e	electron mass
m_r	mass of the rails
N	total number of undulator periods
n_e	beam particle density
P	optical power
P_b	average electron beam power
Q	thermal energy
Q_n	resonator quality factor
q	electric charge of a capacitor
R_c	circuit resistance
R_{ri}	initial rail resistance
R_r	temperature dependent rail resistance
R_p	projectile resistance
R	rail radius
$\dot{r}$	field point displacement from source
r_b	electron beam radius
S	resonator cavity length
T	rail temperature

t	time
t_f	time when projectile exits barrel
v	projectile velocity
w	width between the rails
w_τ	optical mode cross section radius
w_o	optical mode waist radius
X	total length of rails
x	railgun coordinate parallel to projectile displacement
y	railgun coordinate perpendicular to projectile displacement along the armature
Z	railgun coordinate perpendicular to rail axis
Z_o	Rayleigh length
z_u	undulator longitudinal length
α	temperature coefficient
β	dimensionless relativistic electron velocity
β_z	longitudinal component of electron velocity
γ	Lorentz factor
ε	electromotive force
ε_L	self induced electromotive force
ζ	electron phase
η	single pass extraction efficiency
λ	optical wavelength
λ_o	undulator wavelength
μ_o	permeability constant
ρ	electrical resistivity of rail material
ν	dimensionless electron phase velocity
τ	dimensionless time
τ_β	electron beam focal point along the length of the undulator
Φ_B	magnetic flux

ϕ optical phase

ω optical frequency

I.   INTRODUCTION

The United States Navy is investing in the research and development of directed energy weapons for use onboard naval surface platforms. However, significant technological hurdles must be overcome before directed energy weapons are proven operationally viable. The overall goal of this thesis is to aid this scientific effort. Specifically, short Rayleigh length free electron laser (FEL) simulations, electromagnetic railgun simulations, and a proposal to mitigate railgun rail gouging are presented.

Chapter II presents the results of a series of FEL simulations that study how variations in the electron beam focal point along the length of the undulator affect optical characteristics. Both the weak and strong optical field cases are explored determining the impact on the optical mode shape, gain, and extraction. Findings show that moderate variations in the electron beam focal point will not significantly degrade optical beam performance or mirror survivability.

Chapter III presents a numerical model of an electromagnetic railgun. Railgun theory, model design, parameters, and results are discussed. Derived from first principles, the program simulates the railgun circuit profile, joule heating of the rails, and the performance of the projectile as it traverses the barrel. The effects of varying rail materials, barrel geometries, and projectile characteristics are discussed. Model results compare favorably with experiments.

Chapter IV proposes a process that *may* significantly delay the onset velocity of gouging in railgun rails. The proposal, which is to laser peen the surface of railgun rails, may increase the rail hardness and lead to a substantial increase in the maximum muzzle speed attainable. The status of testing and evaluation is discussed.

THIS PAGE INTENTIONALLY LEFT BLANK

II.   FREE ELECTRON LASER

A.   INTRODUCTION

In the current global threat environment, the U.S. Navy is shifting emphasis to the littoral combat regions. This increase in proximity to hostile forces has reduced the reaction time available to defend against anti-ship cruise missiles (ASCMs). Over 70 nations have sea and land launched ASCM arsenals, while another 20 nations are capable of launching ASCMs from the air. ASCM technology continues to improve, increasing the speed and accuracy of the missiles, and ship defense systems must be capable of stopping the missiles while preventing damage to the warship. Given that gun and missile technologies have matured and may be nearing the limits of their capability, new methods are being considered. Therefore, directed energy self-defense of ships is being explored as an alternative to the defensive systems onboard Navy ships today.

Numerous types of lasers exist, varying in power, operation, wavelength and complexity.   These include solid state, chemical, and free electron lasers (FEL). Continuous tunability is a key advantage of the FEL over chemical and solid-state lasers. Tunability of the FEL allows the optical light to propagate at wavelengths offering minimal atmospheric absorption, thereby increasing laser beam propagation in difficult maritime environments. Another advantage is that FELs do not have to remove the toxic effluents that accompany chemical lasers or remove waste heat from the lasing medium of a solid-state laser.

B.   BASIC FREE ELECTON LASER THEORY

The FEL creates tunable, coherent radiation for scientific, medical, industrial, and military applications. An accelerated electron beam, traveling near the speed of light, enters an undulator, which is a device that produces a periodic magnetic field using a series of magnets. The magnetic field induces electron beam oscillations in the transverse direction, causing the electrons to emit radiation in the form of light. Subsequent electron passes through the undulator amplify the radiated energy, which is

stored between the mirrors of an optical resonator. One of the mirrors is partially transparent, allowing the light to be extracted. An illustration of the electron beam path is shown in Figure 2.1.
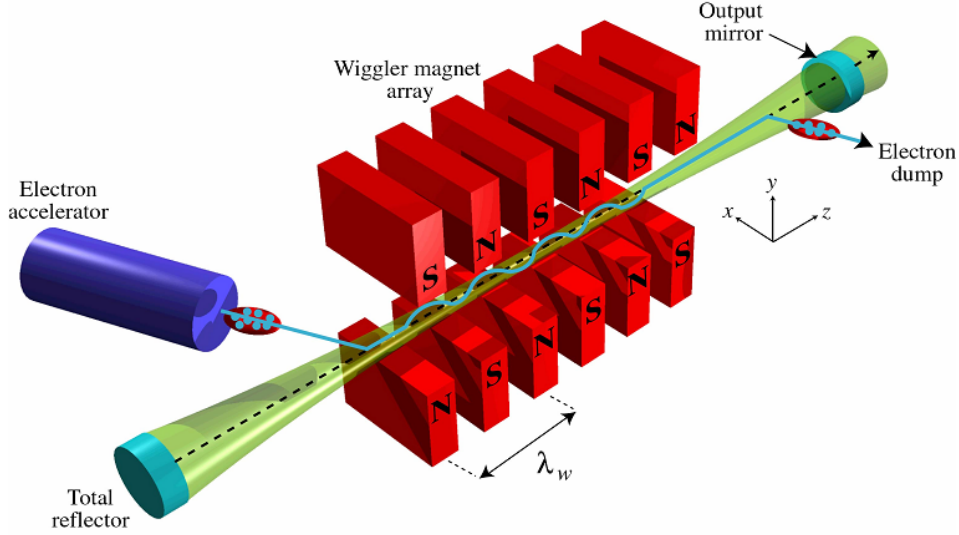
Figure 2.1.   Electron Path Through Undulator and Optical Cavity

Before the electrons reach the undulator, they are accelerated to relativistic energy, $\gamma m_e c^2$, where m_e is the electron rest mass and c is the velocity of light. The Lorentz factor is given as

$$\gamma = \frac{1}{\sqrt{1-\beta^2}} \, ,$$

(2.1)

where $\beta = \upsilon/c$, and υ is the magnitude of the electron velocity.

The electron beam and undulator properties determine the nature of the optical radiation. The magnetic polarization of the undulator, provided either by permanent magnets or by electromagnets, defines the trajectory of the electrons. The magnitude of the electron deflection is determined by the strength of the magnetic field, characterized by the dimensionless undulator parameter

$$K = \frac{eB_{rms}\lambda_o}{2\pi mc^2} \qquad (2.2)$$

where e is the electron charge magnitude, B_{rms} is the root-mean-square magnetic field strength and λ_o is the undulator wavelength. For a typical FEL, $K \approx 1$. The electron beam energy, spacing of the undulator magnets, and magnetic field strength in the undulator determine the wavelength of the optical light.

1.   Resonance Condition

Within the undulator, the position and velocity of the electrons must maintain a certain relationship to the optical and undulator fields to facilitate laser beam amplification. This relationship, called resonance, is the condition that, as an electron travels through one period of the undulator, one wavelength of light passes over the electron (see Figure 2.2).
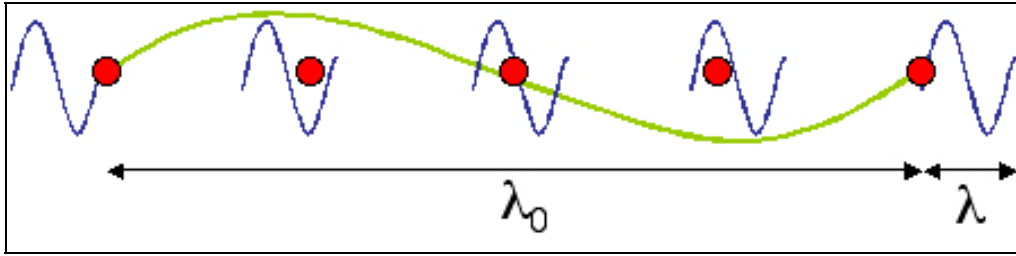
Figure 2.2.   Resonance Condition

As can be seen in Figure 2.2, in the time that an electron (red) moves one undulator period (green), λ_o, the electromagnetic wave (blue) travels a distance of one undulator period plus one optical period, $(\lambda_o + \lambda)$. The distance difference occurs because the electron travels at a speed slightly less than the speed of light. The wavelength of light emitted, which is the difference between distances traveled by the light wave and the electron, can be expressed as [Ref. 1]

$$\lambda \approx \lambda_o \left(\frac{1 + K^2}{2\gamma^2} \right). \qquad (2.3)$$

5

Two of the most attractive features of the FEL are inherent in equation 2.3. First, the FEL is continuously tunable. Changes in the electron energy γmc^2, the magnetic field strength B_m, or the undulator wavelength, λ_o, shift the optical wavelength. Second, the FEL has great design flexibility.

2. Electron Dynamics and the Pendulum Equation

The FEL electron dynamics are described by solving the Lorentz force equations of motion for a single electron in the presence of the undulator magnetic and optical electromagnetic wave fields. The magnetic field for an ideal linearly polarized undulator can be expressed as

$$\dot{B}_m = B_m[0, \sin(k_o z_u), 0], \tag{2.4}$$

where B_m is the peak magnetic field strength on the undulator axis, $k_o = 2\pi/\lambda_o$ is the undulator wavenumber, and z_u is the distance along the undulator axis. By substituting the magnetic field vector into the Lorentz force equation, using the resonance condition (equation 1.3) and assuming $\gamma \gg 1$, we can obtain the FEL pendulum equation.

Many features of the dynamics of the FEL can be modeled using the simple pendulum equation. This simplification is possible because the electromagnetic wave and the magnetic field of the undulator act in tandem on the electrons to produce a sinusoidal potential similar to that of a pendulum in a gravitational field. Therefore, the evolution of an electron in the undulator can be expressed as

$$\overset{\infty}{\zeta} = \overset{\circ}{\upsilon} = |a_o| \cos(\zeta + \phi) \tag{2.5}$$

where the electron phase is $\zeta = (k - k_o)z_u - \omega t$, k is the optical wavenumber, ω is the optical frequency, $\upsilon(\tau) = \overset{\circ}{\zeta} = L_u[(k + k_o)\beta_z - k]$ is the dimensionless phase velocity of the electron, $|a_o| = 4\pi NeKL_u E_s/\gamma^2 mc^2$ is the magnitude of the dimensionless optical field, ϕ is the optical phase, and $\omega = 2\pi c/\lambda$ is the optical frequency. E_s is the optical field magnitude, L_u is the undulator length, and N is the total number of magnetic undulator periods. The notation, $" \overset{\circ}{"} \equiv d""/d\tau$, indicates a derivative with respect to the

6

dimensionless time $\tau = ct/L_u$, where t is the time. Note that $\tau = 0$ at the beginning of the undulator and $\tau = 1$ at the end of the undulator.

The pendulum model is valid for both high and low gain as well as weak or strong optical fields. This model does assume that the fractional energy change of the electron passing through an undulator period is small and that space charge effects are minimal.

3. The Wave Equation

The evolution of the complex optical wave is governed by Maxwell's wave equation driven by the transverse electron beam current. Assuming that the optical field amplitude and phase vary slowly over each optical wavelength, the wave equation can be expressed in dimensionless form as

$$\overset{\circ}{a} = -j < e^{-i\zeta} > \tag{2.6}$$

where j is the dimensionless current density defined by

$$j = 8N\left(e\pi KL_u\right)^2 n_e /\gamma^3 mc^2. \tag{2.7}$$

where n_e is the actual beam particle density. The equation reveals that bunching of electrons around the phase $(\zeta + \phi) \approx \pi$ will lead to amplification of the optical wave, while bunching of the electrons when the phase is near $(\zeta + \phi) \approx \pi/2$ will drive the optical phase.

4. Gain and Extraction

Optical gain, G, which is defined as the fractional increase in optical power per pass, can be expressed as the following

$$G = \left[\frac{a_f^2 - a_o^2}{a_o^2}\right] \tag{2.8}$$

where $a_o = a(0)$ is the initial dimensionless field amplitude and $a_f = a(1)$ is the optical field strength at the end of the undulator where $\tau = 1$. Gain results from when the FEL

7

removes energy from the electron beam and adds it to the optical beam so that a decrease in electron beam energy results in an increase in optical beam energy.

Extraction, η, is the fraction of energy transferred from the electron beam to the optical beam in a single undulator pass and is expressed as

$$\eta = \frac{[E_o - E_f]}{E_o},$$ (2.9)

where E_o is the initial average electron beam energy and E_f is the final average electron beam energy after one undulator pass.

C.   FREE ELECTRON LASER SIMULATIONS

A large number of numerical simulations were conducted to model the performance of the optical mode, gain, and extraction for longitudinal variations in the electron beam focal point within the undulator.   This work is a portion of a larger effort at the Naval Postgraduate School to improve the understanding of FELs though numerical modeling.   The simulations were based upon the classical FEL theory discussed in the previous section. They have been validated with many experiments, and they run on personal computers.

1.   Parameters

The simulations model a short Rayleigh length FEL design, often referred to as a "compact" FEL.   The Rayleigh length, Z_o, is the characteristic distance in which the optical beam increases its cross-sectional area. For a short Rayleigh length FEL, the optical mode radius determined by the resonator with Rayleigh length Z_o and wavelength λ is given by

$$w_\tau^2(z) = w_o^2 \left[1 + \left(\frac{\lambda z}{\pi w_o^2} \right)^2 \right] = w_o^2 \left[1 + \left(\frac{z}{Z_o} \right)^2 \right],$$ (2.8)

where $w_\tau(z)$ is the mode radius at position z along the undulator axis and w_o is the waist radius of the optical mode, and $Z_o \lambda = \pi w_o^2$.   The Rayleigh length is determined by the

8

curvature of the mirrors. A small radius of mirror curvature results in a short Rayleigh length. A short Rayleigh length allows the separation distance of the resonator mirrors to decrease because the optical beam intensity on the mirrors is decreased, thus improving compatibility with the space limitations on ships. Another design benefit is that a shortened Rayleigh length results in greater focusing which allows for amplification of a single optical wave front, which increases optical beam quality [Ref. 2].

For the simulations conducted, the Raleigh length was set to Z_o = 6 cm, in this "compact" FEL, where the full system volume is 20 m x 4 m x 4 m. The undulator length is L_u = 52 cm with a undulator period of λ_o = 2.36 cm, a peak magnetic field strength of B_m = 0.7 T, and the undulator parameter of K = 1.05. The transverse gap between the magnets is 1 cm.

The energy of the electron beam is E = 80 MeV carrying a peak current of I_{peak} = 400 A for each micropulse. Given a micropulse length of l_b =0.15 mm, the average current was I_{ave} = 0.15 A at 750 MHz pulse repetition frequency, producing an average electron beam power of P_b = 12 MW. The electron beam radius was r_b =0.06 mm in the undulator.

The optical beam has a wavelength of λ = 1 μm, a resonator cavity length of S = 18 m, and an optical mode cross-sectional waist radius of w_o = 0.14 mm. A resonator quality factor of Q_n = 4 was assumed, corresponding to 25% mirror output coupling per pass.

2.   Method

The three-dimensional model employed allows multiple transverse optical modes. The simulations account for diffraction and optical wavefront evolution. In each study, the normalized electron beam focal point in the undulator, τ_β, was varied from 0 → 1 in increments of 0.1. For τ_β = 0, the electron beam is focused at the beginning of the undulator (τ = 0), and for τ_β = 1, the electron beam is focused at the end of the undulator (τ = 1). For each τ_β, electron phase velocity ν_o is varied to find the optimum optical gain in weak fields or the optimum extraction in strong fields. The optical beam width at the mirrors and at the undulator center were measured. Figure 2.3 shows a two dimensional

display of a fundamental optical mode in strong optical fields. The horizontal axis, *z*, which is centered on the undulator, is a distance of $3L_u$ long. The vertical axis shows a cross-section through the transverse *y* direction. The positions of sample electrons are depicted in red along the length of the undulator (the ends of which are indicated by the green tick marks) and the white lines mark where the optical field amplitude is 5% of the maximum. At left and right edges of the figure, the theoretical cross-section of optical mode at the mirrors is indicated in purple, while the mode shape found in the simulation is depicted in white. The outcoupling mirror is on the right side of the figure.
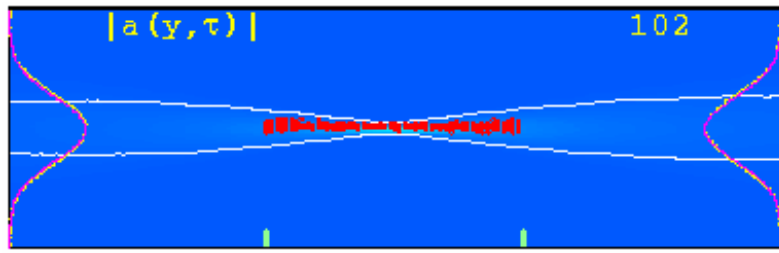
Figure 2.3. **Simulation Result Depicting the Election Beam Focus in the Lasing Cavity.**

3. Results

a. *Weak Fields*

Weak fields occur when the FEL starts up from spontaneous emission, and the magnitude of the optical field strength is small $\left(|a| \leq \pi\right)$ relative to the field near saturation. Simulation runs were conducted in which the initial electron phase velocity v_o was varied at each value of τ_β in order to determine the maximum weak-field gain. Consistent with earlier studies [Ref. 3], results show that the maximum gain is obtained when the electron beam is focused at the center of the undulator in Figure 2.4. When $\tau_\beta \approx$ 0.5, the focus matches the focus of the optical mode, allowing for maximum coupling with the electrons. All the gains observed are far above the threshold output coupling of 25%.
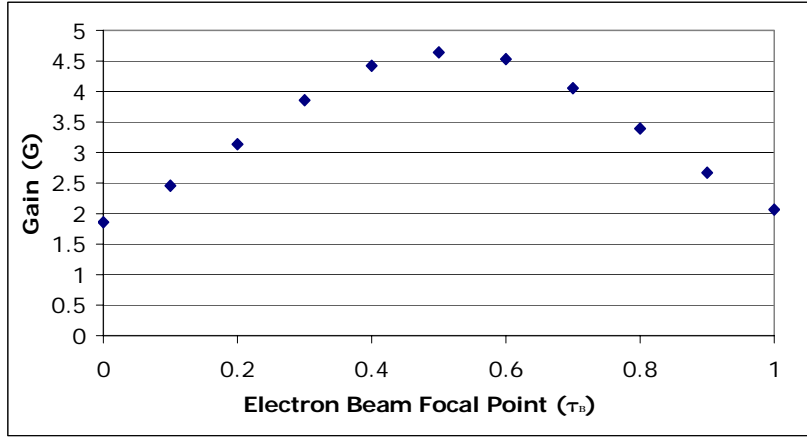
Figure 2.4. **Gain vs. Electron Beam Focal Point (weak field)**

The optical beam width at the mirrors was analyzed for each τ_β where ν_o was again selected to produce the maximum gain. The ratio of the resulting optical mode width to the theoretical width (referred to as the "optical beam ratio") is plotted vs. τ_β in Figure 2.5. The ratio remained nearly constant for all the electron beam focal positions, τ_β, and is only ≈0.6 (≈60%) of the theoretical mode width. Because of the large gain/pass (~400%), the narrower electron beam determines the narrower optical mode width instead of the mirrors.
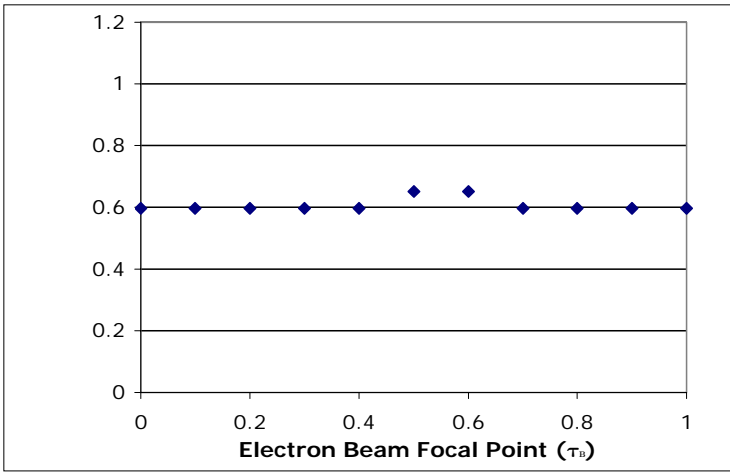
Figure 2.5. **Weak Field Optical Beam Ratio (mirror) vs. τ_β**

11

Similar to the previous study, the optical mode ratio at the center of the undulator was analyzed for each τ_β where ν_o was again optimized to produce optimum gain shown in Figure 2.6. The optical beam ratio varied significantly and was at a minimum value when τ_β was at the center of the undulator. The optical beam in the middle of the undulator was approximately twice the size expected theoretically when the electron beam is focused at either end of the undulator ($\tau_\beta \approx 0$ or $\tau_\beta \approx 1$). The diffracting optical mode expands away from the electron beam focus location in each case, so that the mode is wider at the undulator center ($\tau_\beta \approx 0.5$) when the electron beam focus is farther away. When the electrons are focused at the undulator center ($\tau \approx 0.5$), then the optical mode is smaller there.
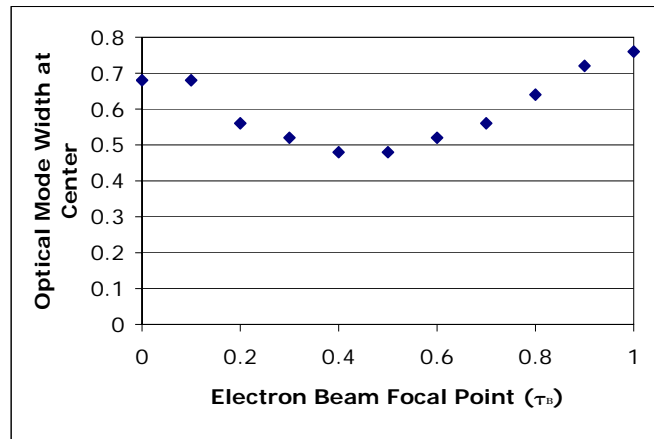
Figure 2.6.   Weak Field Optical Mode Width (undulator center) vs. τ_β

b.   Strong Fields

At saturation, the FEL has strong optical fields. In the simulations, the initial dimensionless electron phase velocity, ν_o, was again varied to determine the optimal extraction for a given τ_β. Results show that the maximum extraction is obtained when the electron beam is focused at the center of the undulator as shown in Figure 2.7. Similar to the optical gain in weak fields, the strong field extraction maximum is not sharply peaked. Given that an approximate extraction of $\eta \approx 2.9\%$ is needed to obtain the desired optical beam output power in excess of $P \approx 300$ kW, it is concluded that

significant variation of the electron beam focal point ($0.3 < \tau_\beta > 0.7$) is tolerable to maintain the desired output power.
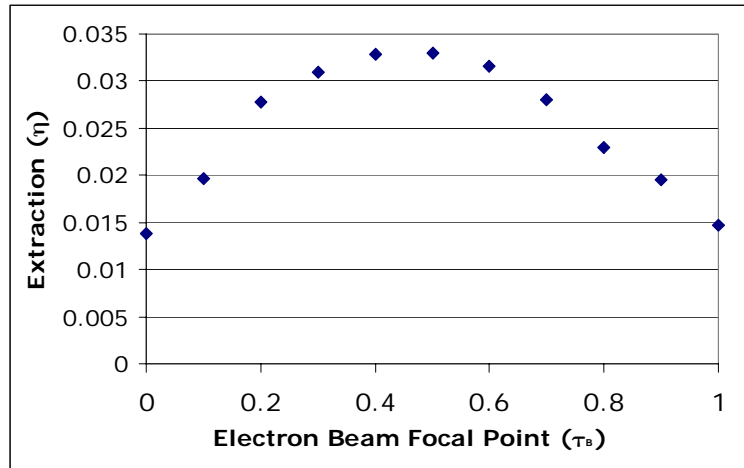

Figure 2.7.   **Extraction vs. Electron Beam Focal Point (strong fields)**

The optical beam ratio at the mirrors was examined to determine its variance with respect to the electron beam focal point. Variations through the entire undulator length caused only minimal deviations as shown in Figure 2.8. Therefore, given that the optical beam intensity on the mirrors is not strongly dependent on τ_β, deviations in τ_β should not significantly impact mirror survivability. At saturation in strong optical fields, the gain/pass is reduced to equal the out-coupling loss, and is only ~25%/pass. For smaller gain/pass, the mirrors dominate the mode structure so that changing τ_β has little effect, as observed.

Figure 2.8. Optical Beam Width at the Mirrors vs. τ_β (strong field)

III. ELECTROMAGNETIC RAILGUN THEORY AND SIMULATION

A. INTRODUCTION

The electromagnetic (EM) railgun is currently being evaluated for Naval Surface Gunfire Support (NSGS) applications for ranges up to 550 kilometers. With velocities in excess of 2000 meters per second, railgun munitions may exceed the current NSGS range by well over an order of magnitude. Such ranges would significantly 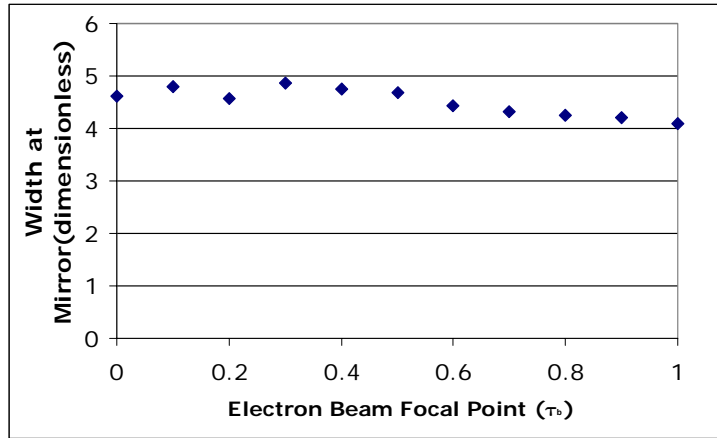extend U.S. naval force projection within littoral combat regions and meet new Marine Corps NSGS requirements during amphibious assaults (as illustrated in Figure 3.1). Because the kinetic energy that railgun munitions would deliver on target would exceed that of conventional projectiles, lethality per salvo should also increase. With greater standoff distances and the elimination of warhead and propulsion charges onboard, ship survivability would improve. Other potential advantages over chemically propelled munitions include significant decreases in: a) projectile delivery time, b) overall cost relative to the current NSGS system, and c) maintenance hours by ships crew. Further, because explosive chemicals would no longer be needed, the hazards involved in their storage and transportation would be eliminated both on and off board. Other applications that may be considered in the future include surface, air and missile ship self defense.

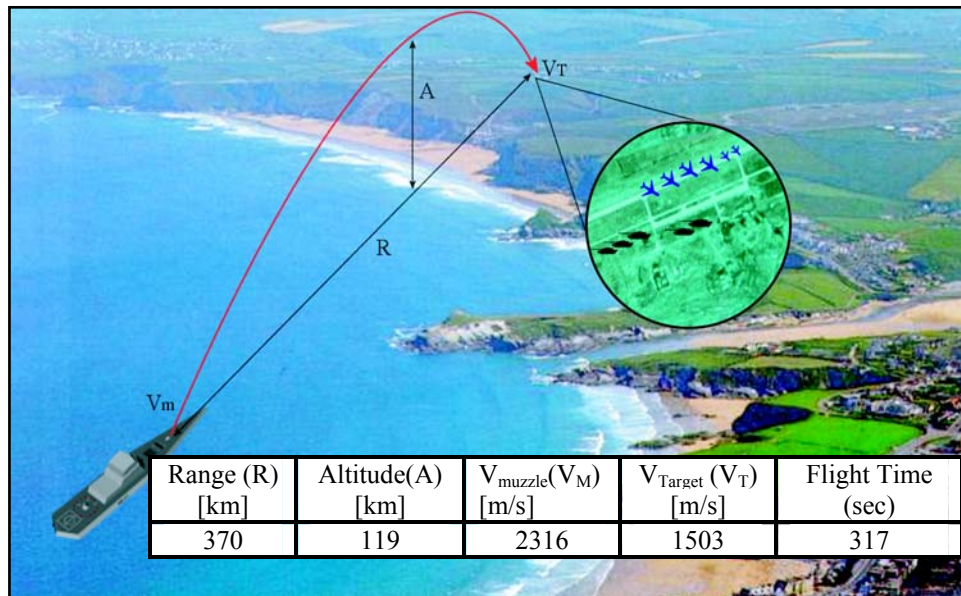

Range (R) [km]	Altitude(A) [km]	$V_{muzzle}(V_M)$ [m/s]	V_{Target} (V_T) [m/s]	Flight Time (sec)
370	119	2316	1503	317

Figure 3.1.   Naval Surface Gunfire Support Concept (from McNabb, IAT)

The advent of the electrically driven warship, which is scheduled to be installed onboard the DD-X platform, has proven to be the catalyst for the development of railgun technologies within the United States Navy. The Integrated Power System (IPS) will be able to provide sufficient power for a railgun onboard naval vessels. However, pulsed power technology must continue to mature to be able to harness the energy from the IPS and release it with sufficient power to drive the railgun. Figure 3.2 illustrates the macro-scale design for a typical IPS system.
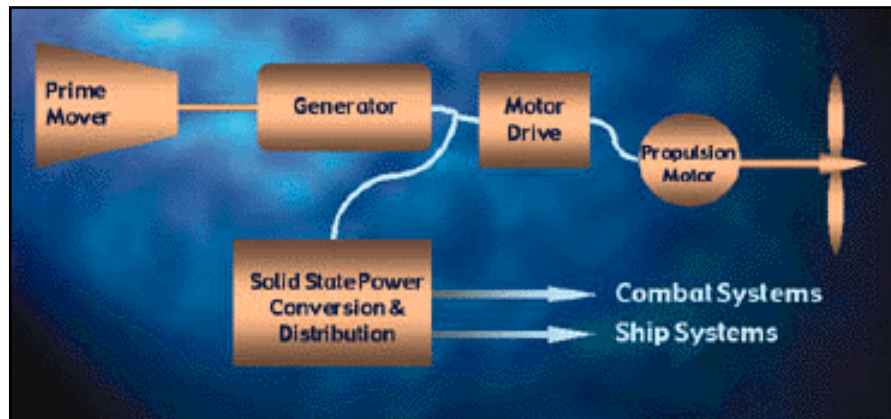
Figure 3.2.   Integrated Power System Schematic (from NSWC Dahlgren)

B.   LETHALITY

While a large database exists to assess hypervelocity kinetic energy (KE) lethality in most direct fire engagement scenarios, relatively little data is available for NSGS. Traditionally, lethality in artillery applications is primarily achieved with high explosive (HE) warheads, which generate a large number of fragments as a result of the blast. The lethality from HE projectiles is mostly due to the KE of the fragments traveling at an average velocity of around 900 m/s. Since the velocities of (non HE) KE warheads are greater and directionality is inherent in their operation, they are expected to have greater lethality than HE warheads for similar impact velocity and fragment (or flechette) size and distributions. The flechette impact velocity will be sufficiently high (even after deceleration during post-deployment flight), that equal or greater lethality should be possible with KE projectiles, provided the sub-munitions can be distributed as required.

A simple estimate of kinetic energy provided by a railgun can be made. If the proposed specifications for a future naval railgun are met, the projectile would deliver roughly 17 MJ of energy on target. In comparison, the kinetic energy delivered on target for the Extended Range Guided Munitions (ERGM) is approximately 6.6 MJ, accounting for energy transferred from the primary explosive to fragments. However, as discussed above, these energies cannot be directly compared in terms of lethality.

C.   PROJECTILE AND ARMATURE

To better understand the constraints placed on the subsequent simulations, a discussion of the physical limitations of the projectile and armature is needed. Because the barrage-round sized aerodynamic package (figure 3.3) is launched with a muzzle velocity in excess of 2000 m/s, survivability becomes a chief concern. Based on currently known limitations in the GPS components in the Navy-developed barrage round, the peak acceleration of the launch package in the barrel has been limited to 30,000 to 40,000 g. Currently, the maximum sustainable acceleration that guidance package electronics are able to sustain is 24,000 g [Ref. 3]. Further, because the shorter the rail length, the higher the acceleration experienced by the projectile, the approximate barrel length must exceed 10 meters. Given the state of technology, the mass of the projectile is limited to about 20 kg. However, this projectile must meet the missions of current conventional rounds including bunker penetration, anti-personnel, and armor piercing operations.

In contrast to Army applications, the lower accelerations in the Navy railgun will allow the armature to push the projectile at its base, rather than the round's midsection. An added benefit of the base-push approach is that it is likely to be much more robust in the event of arcing at the rail-armature interface. It is unlikely that disruptive transition pressures would be transmitted to the projectile package, as can occur when launching a long rod with the mid-riding sabot, sometimes leading to break-up of the rod.

Figure 3.3. Experimental Barrage Round

C. ENERGY STORAGE DEVICES

Due to the elimination of propellants from the gun system, pulsed electrical power of tens of GWs has to be provided to the railgun during the projectile launch duration (typically about ten milliseconds). Any energy storage device chosen to drive the railgun must be able to provide enough power for 6-12 launches per minute. Several potential power sources are currently being considered, each using different physical principles: capacitors (electrostatic); pulsed alternators (inertial); inductors (magnetic); and batteries (chemical).

1. Capacitors

Capacitors have among the highest energy densities of any energy storage mechanisms. Widely used in industry today, capacitors have been demonstrated to have energy densities in excess of 2.5 MJ/m^3. Although some research is taking place to develop new dielectric materials, only limited funding is available and it is not yet clear what capacitor technology will be available for a future ship. Present capacitor technology may be acceptable in size and weight for a DD-X class of destroyer.
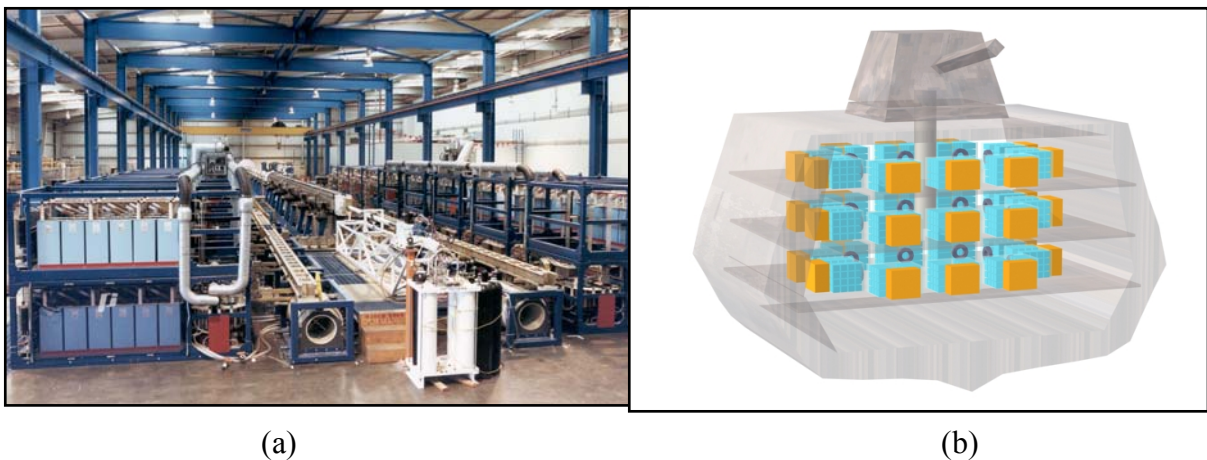

(a)   (b)

Figure 3.4. Capacitors: (a) a 32 MJ Capacitor Bank, (b) a Potential 200 MJ System Laid Out in a DD-X Hull Section

18

2. Alternators

Though not as mature as capacitors, rotating machines have many advantages, including high energy density, reliability, and their ability to store energy for long periods of time without significant reduction in their lifespan. Arranged in counter-rotating pairs to mitigate torque reaction forces, alternators may be the optimum energy storage device in terms of space and weight management onboard naval vessels. They have the flexibility to operate at different energy levels, which translates into different projectile ranges and/or masses, leading to a robust armament in for addressing various battle scenarios. The stored energy is discharged inertially in the pulsed alternators. Prior to the next shot, the energy used has to be re-stored by spinning up the machine rotors back to their initial speed using electric motors. Separate motors could be used but would require the use of gearboxes and clutches. A better solution is to design the pulsed alternator so that a motor is embedded in the rotor/stator structure: two potential approaches of this type are shown in Figure 5.
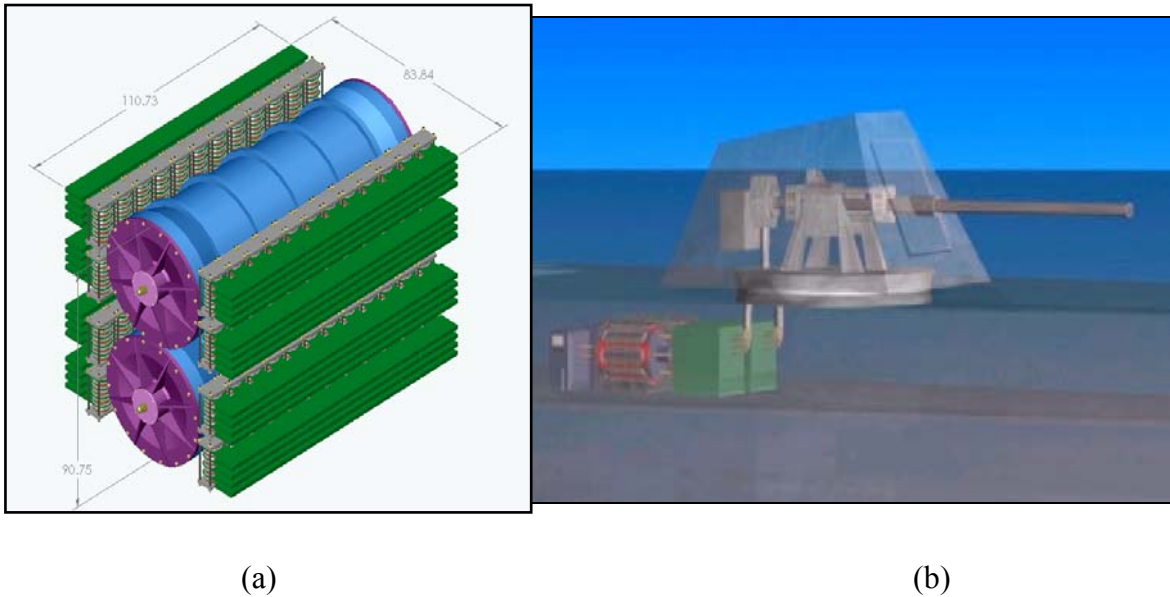

(a)   (b)

Figure 3.5.   Alternators: (a) Conceptual Design for Contra-rotating Pulsed Motor-generators and (b) a Potential Multi-Alternator Layout in a Ship.

3. Battery/Inductor System

Batteries are very effective at storing energy and are widely used in the Navy. However, they are not capable of delivering power at the rate required for a large railgun. Several early railgun systems were successfully operated using an intermediate inductive energy storage system, and future work will continue to evaluate this approach for the Navy. This arrangement would utilize batteries to charge up an inductive circuit (one or more large coils) that can then be discharged into the railgun at the required power levels. This pulse compression arrangement ensures that even though the power delivered into the railgun breech might be 10 GW over 10 milliseconds, the batteries could recharge the inductor over five seconds at a rate of 25 MW. The advantage of this arrangement is that it is smaller, it operates at lower voltages than capacitors, and there is no rotating machinery. However, a special switch is needed to open the railgun current and provide the current pulse. Such switches are not available now, but some research is underway.

D. SIMPLIFIED RAILGUN

Prior to exploring the theory of the railgun in detail, it is instructive to examine a simplified case. In this section, rough approximations will be used to illustrate some of the most important railgun concepts and characteristics.

Fundamentally, the goal of any railgun is to convert electromagnetic energy into kinetic energy imparted on a projectile. When current flows through the rails of a railgun, a magnetic field is produced. The current also flows through the projectile, which thereby experiences a force due to the magnetic field. In general, the magnetic field at a given point due to current within a circuit can be expressed using the Biot-Savart Law

$$d\vec{B} = \frac{\mu_0}{4\pi} \frac{I d\vec{l} \times \vec{r}}{r^3}, \tag{3.1}$$

where μ_o is the permeability constant, I is the current, $d\vec{l}$ is the length vector element in the direction of the current, and $\vec{r}$ is displacement of the field point from the source. In

the case of the railgun, the magnetic field created due to the current through each rail can be approximated by considering each rail to be a semi-infinite wire of radius R separated by width w.
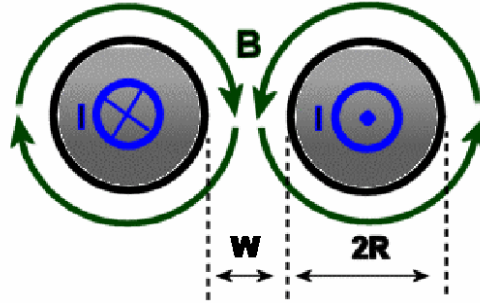
Figure 3.6. **Cross-sectional view of the rails**

Thus, from Amperes' Law, the magnetic field due to a single semi-infinite rail can be expressed as

$$B = \frac{\mu_o I}{4\pi r}. \tag{3.2}$$

If the distance w is small compared to the rail radius, then the magnetic field between the rails can be considered constant. With this approximation, and because the magnetic field doubles when both rails are taken into account, the magnetic field, B, experienced by the projectile now becomes

$$B = \frac{\mu_o I}{2\pi R}. \tag{3.3}$$

This field exerts a force on the current through the projectile within the circuit according to the Lorentz force equation

$$\vec{F}_L = I\vec{l} \times \vec{B}, \tag{3.4}$$

\where $\dot{F}_L$ is the Lorentz force and $\dot{l}$ is the length in which the current travels. For this case, $l = w$ which is the distance between the rails. Using equation 3.4 to obtain the magnitude of $\dot{F}_L$ and noting that the angle between $\dot{B}$ and $\dot{l}$ is 90°, we can write

$$F_L = IwB \sin 90° = IwB \qquad (3.5)$$

By substituting equation 3.3 for the magnetic field, the force induced on the projectile can now be expressed as

$$F_L = \frac{\mu_o I^2 w}{2\pi R} \qquad . \qquad (3.6)$$

It is this force that accelerates the projectile out of the barrel, providing the desired kinetic energy. Using Newton's second law, the constant acceleration, a, is

$$a = \frac{F_L}{m} = \frac{\mu_o I^2 w}{2\pi m R}, \qquad (3.7)$$

where m is the mass of the projectile. The velocity of the projectile v, is therefore

$$v = \int a \, dt = \frac{\mu_o I^2 wt}{2\pi m R}, \qquad (3.8)$$

where t is time. By integrating again, the position of the projectile along the rail for a given time

$$x = \int v \, dt = \frac{\mu_o I^2 wt^2}{4\pi m R}. \qquad (3.9)$$

Many important concepts emerge from this simple derivation. The force, and therefore the acceleration and velocity of the projectile increase in proportion to I^2. The

acceleration and velocity increase in proportional to the distance between the rails or width of the projectile, and decrease proportionally with the mass of the projectile and rail radius.

At this stage, an analytical evaluation of the performance characteristics of the projectile is useful to develop a feel for the magnitude of the values a railgun can produce. Using the proposed railgun parameters established by the Navy (Table 3.1) coupled with $R = 0.1$ m and $w = 0.01$ m, the performance characteristics for the proposed naval railgun can be roughly approximated.

Metric	Symbol	Value
Average Input Current	I	5 MA
Projectile Mass	m	20 kg
Rail Length	X	10 m

Table 3.1.   Proposed Metrics for Naval Railgun

Using equation 3.7, the acceleration can be found to be $a=5\mathrm{x}10^5$ m/s^2. Using the following expression

$$t_f = \sqrt{\frac{2X}{a}},$$
(3.10)

where X is the total length of the barrel, the total time of acceleration is t_f, = 6.3 milliseconds. By using the following equation,

$$v = \sqrt{2aX},$$
(3.11)

the exit velocity of the projectile is found to be v=3.2 km/s, and the kinetic energy, KE, is

$$KE = \frac{1}{2}mv^2.$$
(3.12)

This idealized projectile would carry about 100 MJ of energy upon exiting the barrel!

It is important to state that, although these values are impressive, an array of complications that have not yet been considered, such as resistance, inductance, and impedance, will reduce the exit velocity. In subsequent sections, these complications will be addressed in detail to develop a parametric model capable of more accurately simulating many characteristics of the proposed naval railgun.

E.   VARIABLE MAGNETIC FIELD

In Section 3.E, we took the magnetic field along the width of the projectile as constant by considering the distance between the rails, and therefore the projectile width, to be much less than the radius of the rails. However, the projectile width and rail size are comparable. To more accurately evaluate the force imparted on the projectile, we will now derive the Lorentz force given a rail geometry similar to the proposed naval railgun.
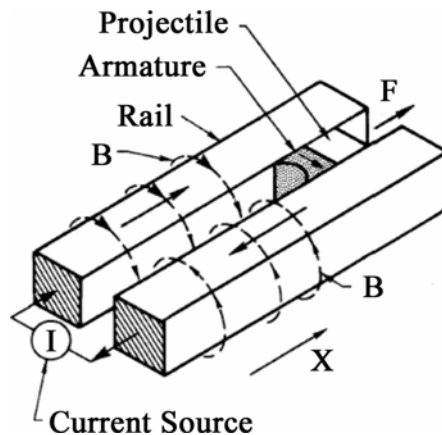

Figure 3.7.   Typical Rail Geometry (from Lawrence Livermore National Laboratory)

Using equation 3.4 and inserting the magnetic field from equation 3.2, the differential form of the Lorentz force vector, $d\vec{F}_{L1}$, due to the magnetic field of a single rail at a given distance, y, from the center of the rail can be expressed as

24

$$\vec{dF}_{L1} = I\left(dz\,\vec{k}\right) \times \vec{B}_1 = I\left(dz\,\vec{k}\right) \times \left(\frac{\mu_o I}{4\pi z}(-\vec{j})\right) = \frac{\mu_o I^2}{4\pi z}dz\,\vec{i} \; . \tag{3.13}$$

where dz is an element of length along the projectile width. By integration across the projectile to obtain the total force, we find

$$\vec{F}_{L1} = \int \vec{dF}_{L1} = \frac{\mu_o I^2}{4\pi}\int_R^{R+w}\frac{1}{z}dz\,\vec{i} = \frac{\mu_o I^2}{4\pi}\ln\!\left(\frac{R+w}{R}\right)\vec{i} \; . \tag{3.14}$$

To obtain the magnetic field contributions from both rails, the law of superposition applies, doubling the force obtained above. The Lorentz force imparted on the projectile becomes

$$\vec{F}_L = \frac{\mu_o I^2}{2\pi}\ln\!\left(\frac{R+w}{R}\right)\vec{i} \; . \tag{3.15}$$

The acceleration of a projectile with mass m is

$$a = \frac{\mu_o I^2}{2\pi m}\ln\!\left(\frac{R+w}{R}\right) . \tag{3.16}$$

For $w<<R$, as assumed in the last section, $\ln(1+w/R) \approx w/R$, and we recover equation (3.7) for the projectile acceleration. By integrating equation 3.16 over time t, the velocity is

$$v = \frac{\mu_o I^2 t}{2\pi m}\ln\!\left(\frac{R+w}{R}\right) , \tag{3.17}$$

and the position of the projectile becomes

$$x = \frac{\mu_o I^2 t^2}{4\pi m}\ln\!\left(\frac{R+w}{R}\right) . \tag{3.18}$$

To analyze the performance of the railgun and the effects of realistic rail dimensions, the input data from Tables 3.1 and 3.2 was used.

Metric	Symbol	Value
Distance between Rails	w	0.2 m
Radius of Rails	R	0.1 m

Table 3.2.   Additional Metrics for NSGS Railgun

Figure 3.8 is a graphical display of the projectile's velocity as it translates the length of the barrel. Notice that the final velocity is reduced from $v_f \approx 3.2$ km/s found earlier to less than 2.5 km/s because of the larger projectile size (w=0.2 m instead of w=0.01 m). The interior parts of the larger projectile are further from the rail centers and experience a reduced force.
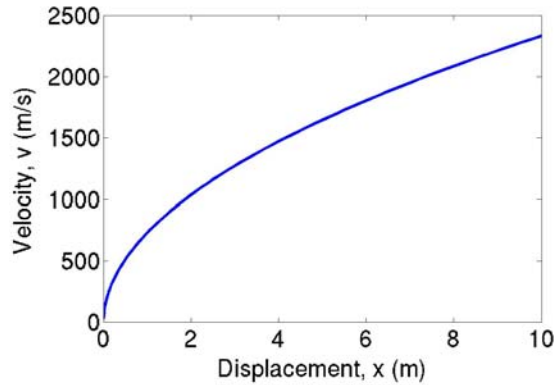
Figure 3.8.   Velocity vs. Displacement for w=0.2 m, $R = 0.1$ m

To illustrate the influence that rail geometry has on the projectile's velocity, the values of w and R were changed to w=0.1 m and R=0.2 m, respectively. The new results can be seen in figure 3.9. The simulation predicts a nearly 1.0 km/sec decrease in muzzle velocity when R is doubled while w is halved. This occurs because increasing the rail radius causes a decreased magnetic field strength across the projectile/armature. Additionally, by decreasing the width between the rails, the magnetic field has less area

26

on which to exert force on the armature/projectile. These combined factors cause the dramatic decrease in the muzzle velocity.

Figure 3.9.   Velocity vs. Displacement for *w*=0.1 m, *R* = 0.2 m

F.   COMPLEX RAILGUN THEORY

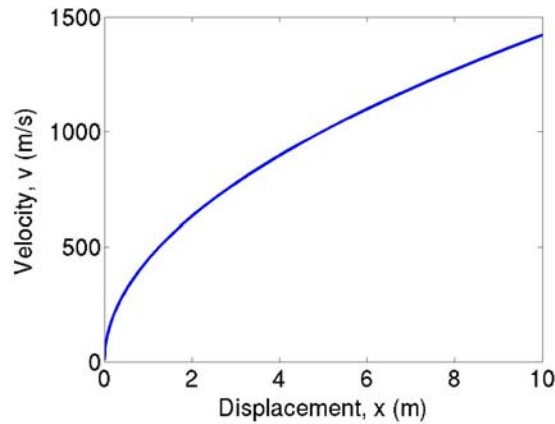To this point, the current in the railgun circuit has been considered constant. However, in reality, the current, *I(t)*, changes in time and depends on the source voltage, circuit inductances, resistances, and heating. This section introduces the concepts needed to model *I(t)* more accurately.   The basic physics remains the same and the Lorentz force equation obtained in equation 3.15 is used to calculate the equations of motion in the model.

1.   Rail Inductance

The generalized equation for magnetic flux is

$$\Phi_B = \int \vec{B} \cdot d\vec{A}, \tag{319}$$

where $d\vec{A}$ is the area vector element which in this case is normal to the magnetic field $\vec{B}$. To obtain the magnetic flux due to one rail, the geometries and orientation from figures 3.6 and 3.7 are used to define the area that the magnetic field (obtained from equation 3.2) influences. Integrating the magnetic field $B=\mu_o I/4\pi z$ due to one rail over the element of interior area of the railgun, $dA = x dz$, the flux is

27

$$\Phi_B = \int BdA = \int \left(\frac{\mu_o I}{4\pi z}\right)xdz = \frac{\mu_0 Ix}{4\pi}\int_R^{R+w}\frac{dz}{z} = \frac{\mu_0 Ix}{4\pi}\ln\left(\frac{R+w}{R}\right), \tag{3.20}$$

where w is the distance between the rails, R is the radius of each rail, z is the distance across the projectile, dz is an element of that distance, and x is the distance along the rails. Due to the principle of superposition, when considering the contribution from *both* rails, the magnetic flux increases by a factor of 2. By definition, the rail inductance for a single loop is then

$$L_r = \frac{\Phi_B}{I}. \tag{3.21}$$

Substituting the magnetic flux, the railgun barrel inductance is

$$L_r = \frac{\Phi_B}{I} = \frac{\mu_0 x}{2\pi}\ln\left(\frac{R+w}{R}\right), \tag{3.22}$$

Note that the rail inductance increases as the projectile moves along the rail and creates a magnetic field over a larger area xw.

2. Rail Resistance

The electrical resistance in the rails depends on the projectile displacement, temperature, and current. It significantly influences the railgun circuit performance and therefore affects the projectile acceleration and rail heating characteristics. By tailoring the general expression for electrical resistance, the temperature-independent rail resistance, R_{ri}, is

$$R_{ri} = \frac{2\rho x}{A_{cs}} \tag{3.23}$$

where ρ is the electrical resistivity of the material, A_{cs} is the area perpendicular to the current flow and the factor of two accounts for the resistance of both rails. A_{cs}, which is

the product of the rail width $w = 0.2$ m, and height $h = 0.2$ m was 0.04 m^2 for all simulations unless stated otherwise. Inserting equation 3.23, the temperature-dependent resistance is given by

$$R_r = R_{ri}\left[1 + \alpha(\Delta T)\right] \tag{3.24}$$

where α is the temperature coefficient of resistance and ΔT is the change in temperature of the rails. The above rail resistance can now be included in the current and thermal equations of the simulation, where the temperature will be calculated self-consistently.

In the railgun circuit, the projectile and circuit resistances are approximately two orders of magnitude smaller than the average rail resistance. Therefore, although variations in these values occur during launch, their effects are insignificant for the results explored in this thesis. For this reason, projectile and circuit resistances are assumed to be constant in the model.

3. Circuit Equation

According to Kirchoff's Law, the algebraic sum of the changes in potential of any circuit loop must equal zero. Therefore, to obtain a railgun circuit equation for analysis, a proper determination of all voltage gains and drops must be identified. Figure 3.10 provides a macro-scale schematic of all significant sources of voltage gain/drop within the railgun circuit.
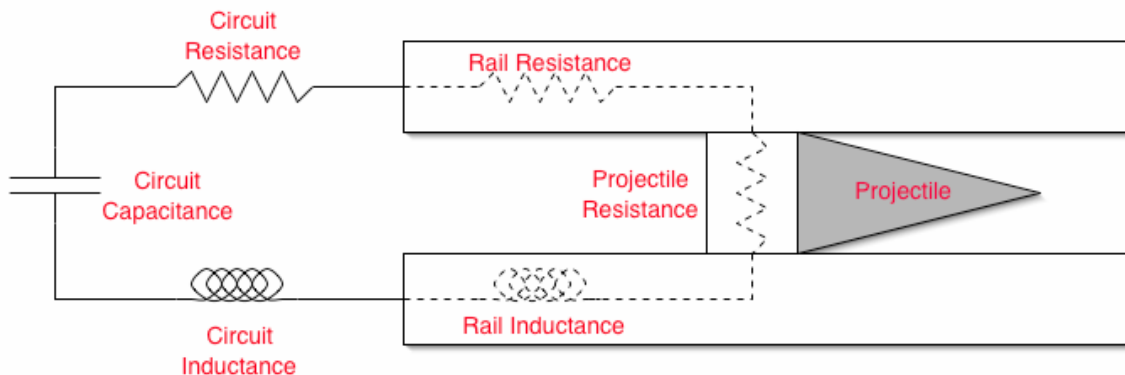

Figure 3.10. Capacitor Driven Railgun Circuit

For this circuit, the capacitor bank provides the energy for the railgun launch. The voltage gain, ε, across the capacitors is

$$\varepsilon = \frac{q}{C},$$
(3.25)

where q is the charge stored by the capacitors and C is the capacitance. In the railgun model, q = 25,000 coulombs and C = 2 farads, resulting in an input energy of 156 MJ . The voltage drop incurred by resistances are given in terms of IR, while the voltage change across an inductive element is

$$\varepsilon_L = \frac{d(LI)}{dt},$$
(3.26)

where R is the generic resistance, I is the current, and L is the electrical inductance. Therefore, the circuit equation, which describes the railgun as shown in figure 3.10, can be written as

$$\frac{q}{C} + R_c I + R_r I + R_p I + L_c \frac{dI}{dt} + \frac{d(L_r I)}{dt} = 0,$$
(3.27)

where R_c, R_r, and R_p are the resistances of the circuit, rails, and projectiles, respectively. In subsequent simulations, the circuit and projectile resistances are R_c = 205 μΩ and R_p = 20 μΩ, whereas the rail resistance is given by equation 3.24. L_c = 5 μH is the circuit inductance while the inductance in the rails, L_r, is given by equation 3.22. By the chain rule, the last term in equation (3.27) becomes

$$\frac{d(L_r I)}{dt} = L_r \frac{dI}{dt} + I \frac{d(L_r)}{dt},$$
(3.28)

where

$$\frac{d(L_r)}{dt} = \frac{d(L'_r x)}{dt} = L'_r \frac{dx}{dt} = L'_r v,$$ (3.29)

and where

$$L'_r \equiv \frac{dL_r}{dx} = \frac{\mu_0}{2\pi} \ln\left(\frac{R+w}{R}\right)$$ (3.30)

is a constant from equation 3.22. The circuit equation now can be expressed as

$$\frac{q}{C} + R_c I + R_r I + R_p I + L_c \frac{dI}{dt} + L_r \frac{dI}{dt} + L'_r v I = 0.$$

(3.31)

We now can solve the circuit equation to obtain the change in current over time (dI/dt).

$$\frac{dI}{dt} = \frac{\left[\frac{q}{C} + I\left(R_c + R_r + R_p + L'_r v\right)\right]}{L_C + L'_r x}.$$ (3.32)

Equation (3.32), together with $I = dq/dt$, are the key equations used in the model.

4.   Joule Heating

Thermal heat induction of the rails due to the intrinsic electrical resistance of the materials must be evaluated to predict their survivability. Excess heat absorption can dramatically reduce the rail lifespan due to melting or excess thermal expansion, which results in plastic deformation.

Neglecting friction, the thermal energy (ΔQ) absorbed by the rails at time t can be expressed as

$$\Delta Q = \int_0^t R_r I^2(t)dt.$$ (3.33)

The change in temperature of the rails is given by

$$\Delta T = \frac{\Delta Q}{m_r c_h}, \tag{3.34}$$

where m_r is the mass of each rail and is given by

$$m_r = \rho_r A_{cs} X, \tag{3.35}$$

c_h is the specific heat of the rail material, and ρ_r is the density of the rail material.

5. Material Properties

Except where specified, copper was selected as the rail material for all subsequent simulations. Table 3.3 shows the material property values used for the materials studied.

Rail Material	Rail Resistiviy ρ ($\Omega \cdot$nm)	Temp. Coeff. of Resistance α (1/K)	Specific Heat C_h (J/kgK)	Rail Density ρ_r (kg/m^3)
Copper	17	4.3×10^{-3}	386	8230
Tungsten	54	4.5×10^{-3}	134	19250
Silver	16	4.1×10^{-3}	236	10490

Table 3.3.   Material Properties

G.   RAILGUN SIMULATIONS

The subsequent simulations predict the circuit, projectile, and thermal performances of a railgun driven by a bank of capacitors discharged in parallel. A finite-difference solution is employed to calculate time-varying elements of the railgun circuit, thus determining the current. From this, performance characteristics such as acceleration, velocity, and displacement can be found as well as changes in resistance and thermal, and kinetic energy. To validate the results, comparisons were made with experimental results achieved at the Instituted for Advanced Technology (IAT) railgun test facility.

1.   Method

In the simulation, copper was chosen as the rail material for the initial series of performance results. The parameters for railgun explored in the subsequent sections are

as follows: The barrel length is X=10 m with a rail radius of R=0.2 m, a height of h=0.2 m, and a separation between the rails of w = 0.15 m. The projectile mass is m=20 kg. The capacitor charge is q=25,000 F with a capacitance of C = 2.0 H. The circuit resistance is R_c = 205 $\mu\Omega$ and the rail resistance is R_p = 20 $\mu\Omega$. The circuit inductance is L_c = 5 μH.

Using equation 3.16, the simulation calculated projectile acceleration, velocity and displacement, using the Euler-Cromer method. In order to prevent oscillations in the LRC circuit, an actual gun will switch off the current flow when the current reaches zero. So, when the change in current reached zero, the charge was also set to zero. In an actual railgun circuit, a diode would be used to shunt the current away from the capacitors and thereby prevent the current from reversing.

2.   Results and Discussion

a.   Current Pulse Formation

By modeling the current pulse of the railgun circuit, a significant amount of data can be obtained to predict overall trends within the system. Figure 3.11 displays the evolution of the current with respect to projectile displacement and time. Ideally, the current pulse would remain constant as the projectile traverses the barrel. This is beneficial for several reasons. Constant current prevents a sharp peak in acceleration, preventing
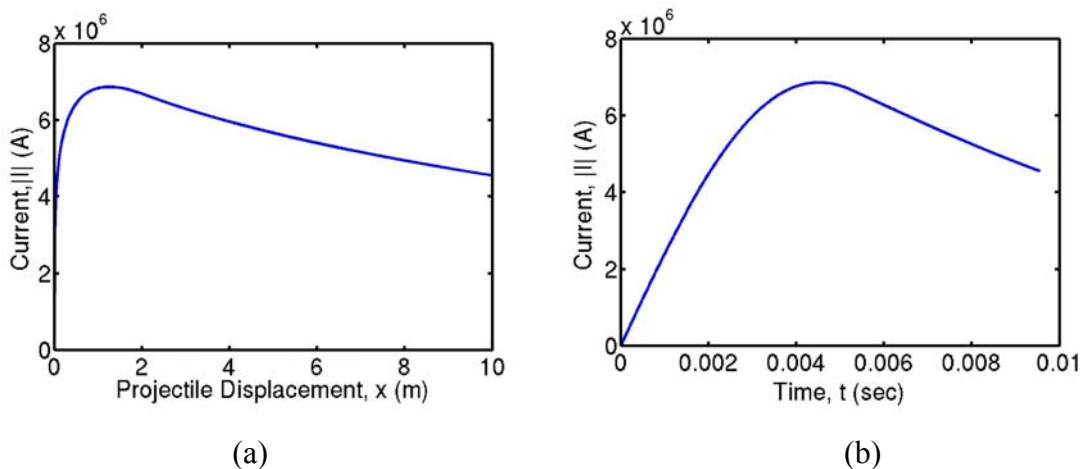

(a)   (b)

Figure 3.11.   Current vs. (a) Displacement and (b) Time for the Notional Naval Railgun

33

possible damage to the guidance package. Also, experiments have shown that rapid decreases in the current pulse can lead to plasma arcing between the rails and armature [2]. As shown above, a single current pulse from a typical capacitor source is very large during launch. High current densities for short durations, as encountered with high peak currents in railguns, also cause more resistive heating to be transferred to the surface and edges of the rails due to the lack of time for diffusion of the electrical current. This effect can cause rail melting and significantly limit the number of rounds that a railgun can fire over a given period of time. For these reasons, multiple current pulses during a single launch with time-delayed discharges are considered preferable. Proper staging of current discharges results in a more constant current (and therefore acceleration).

b. *Projectile Velocity*

With a single pulse discharge, the model predicts a muzzle velocity of approximately 2350 m/sec (Figure 3.12), which is comparable to the desired 2300 km/sec that the Office of Naval Research established as the benchmark for a viable weapon system. The muzzle velocity translates to 55 MJ of kinetic energy imparted on the projectile (the target muzzle energy for the Navy is 63 MJ). Therefore, for 156 MJ of electromagnetic input, 101 MJ goes to waste heat resulting in 33% energy efficiency.

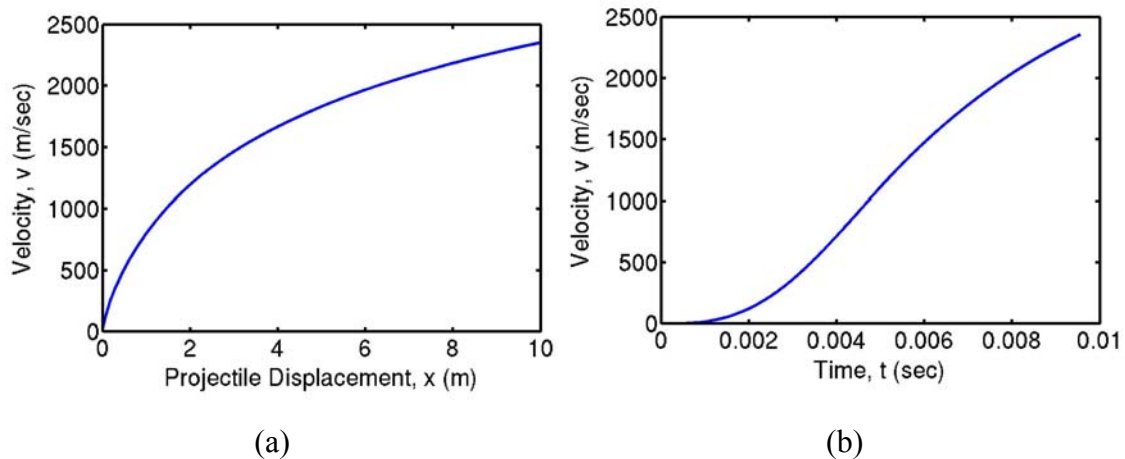(a)   (b)

Figure 3.12.   Velocity vs. (a) Displacement, and (b) Time

Some railgun designs propose to increase the muzzle velocity by pneumatically or chemically accelerating the projectile into the barrel breach prior to the capacitor discharge. A study was conducted to examine the effect that an initial

projectile velocity has on the muzzle velocity. With an initial velocity of $v = 200$ m/s at $t = 0$, the model calculated a muzzle velocity of $v \approx 2350$ m/sec. Significant initial velocities had negligible effect on the final muzzle velocity.

c.   *Acceleration*

The acceleration profile of the projectile is an important characteristic to monitor to determine whether the guidance package can survive the peak acceleration imparted to the projectile. NSWC Dahlgren predicts that, with current technologies, a guidance package would not survive a peak acceleration of greater than 40,000-50,000 g (Petry, 2001, pp. 7). As figure 3.13 illustrates, the peak acceleration in this example approaches the limits on current guidance packages. However, as discussed in section 3.H.2.a, techniques to alter the current profile, and therefore, the acceleration, are being explored by the Navy. Besides staging current pulses, pulse-conditioning techniques to limit the peak acceleration are in development. Increasing the barrel length could reduce the peak acceleration by allowing the current pulse to be diffused over a longer period of time. However, a longer barrel exaggerates other negative effects in the system. The increased length (and accompanying mass) causes greater torque on the turret due to gravity and also leads to greater difficulty in the system's ability to slew and elevate when acquiring a target; especially when rapid acquisition is needed. Also, the mechanical stress caused by the torque, when coupled with high barrel heat, can cause plastic deformation of the barrel.
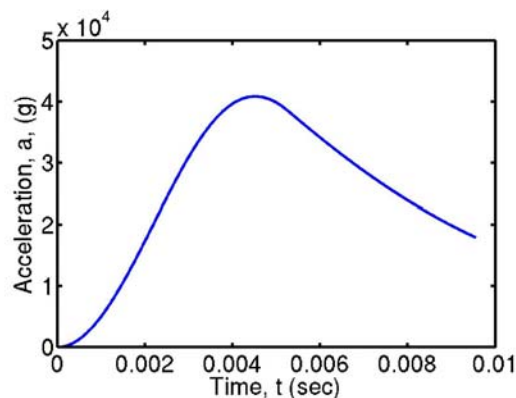

Figure 3.13.   Acceleration vs. Time

d. Rail Resistance and Joule Heating

The resistance of the rails is dependent on several factors including the inherent resistivity of the metal, the magnitude and duration of the current pulse, frictional heating due to surface contact at the rail-armature interface, and the length of the rails. Simulation results show that the increase in rail resistance is nearly proportional to the projectile displacement along the rails. At the end of the launch, the rail resistance is $R_r = 11\ \mu\Omega$. Given that the rail resistance is small compared to the circuit resistance, $R_c = 205\ \mu\Omega$, it did not significantly affect the circuit or projectile performance.

Thermal management of the rails is considered significant given that, at the currents necessary for a Naval railgun, the possibility of rail melting is considerable over many conservative shots. For this model, the thermal energy induced into the rails for any given time step was calculated using the equation

$$dE = R_r I^2 dt. \tag{3.36}$$

For a single launch, the rail temperature is found to only increased by $\Delta T \sim 1$ K. Similar values were also obtained for simulations with tungsten and silver rails. Because $R_c \gg R_r$, the majority of heat loss occurs as the current flows through the circuit resistances. Further, this simulation only accounts for the heat injected into the rails electrically. Active barrel cooling and heating due to frictional forces are unaccounted for. Further, this model does not simulate the open-circuit when the projectile exits the barrel, which prevents the current from completing the circuit path. For theses reasons, resistance and thermal profiles generated by the model can only serve as rough estimates to a real system.

e. Railgun Performance for Various Rail Materials

The Navy is currently in the process of determining the best rail material to use to optimize the railgun performance. Because the rail material chosen affects the resistivity and therefore the current profile within the circuit, depending on design, material selection may significantly impact the muzzle velocity of the projectile. In this section, tungsten and silver rails were chosen (Table 3.3) to study the impact on circuit and projectile performance when compared to copper rails (Section 3.H.2.a). With

tungsten rails, the muzzle velocity of the projectile decreased by only 5 m/sec out of 2350 m/s while silver rails were found to increase the muzzle velocity by only 6 m/sec. The minimal changes in muzzle velocity is consistent with design, where $R_c \gg R_r$.

f. **Projectile Mass Increase Due to Guidance Package**

A guidance package onboard an EM railgun projectile is almost certainly necessary if target accuracy is to be achieved. Additional projectile material, and therefore additional mass, may be necessary to accommodate more effective rounds for different mission profiles. For the purpose of this simulation, an additional 8 kilograms of mass is added to observe the effects on both the muzzle velocity and the kinetic energy with copper rails. The muzzle velocity drops by over 400 meters per second; however, the kinetic energy only drops by ~ 3 MJ. The KE delivered on the target may not decrease substantially because the added mass will decrease drag during the trajectory.
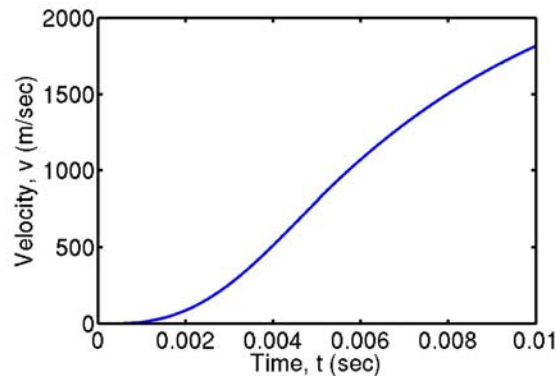

Figure 3.14.   Velocity vs. Time for a 28 kg Launch Package

THIS PAGE INTENTIONALLY LEFT BLANK

IV.   HYPERVELOCITY GOUGING AND ARCING

A.   HYPERVELOCITY GOUGING

Hypervelocity gouging occurs when materials are in sliding contact at high velocity relative to each other.   Hypervelocity gouging (hereafter referred to as "gouging") is a phenomenon known to occur in railgun rails, rocket sled tracks, and gas gun barrels.   Gouges are teardrop-shaped craters in the direction of the velocity vector that limit the useful life of the materials in which they occur and often become the critical life-limiting defect.   It is also a threshold phenomenon; for any given material pair, there is a threshold velocity below which gouging does not occur.

Figure 4.1.   Gouging in Copper Rails (from Stefani, IAT)

Recent studies indicate that the threshold velocity at which gouging occurs is governed by the hardness of the harder material and by the density and sound speed of both materials.   While the density and sound speed characteristics are intrinsic properties of any given material, the hardness of the material can vary significantly, depending on its preparation and history.   Experiments have determined that the gouging threshold velocity is approximately linearly proportional to the hardness (Figure 4.2). Therefore, to alleviate gouging, numerous methods have been proposed to increase the hardness of the rail material.
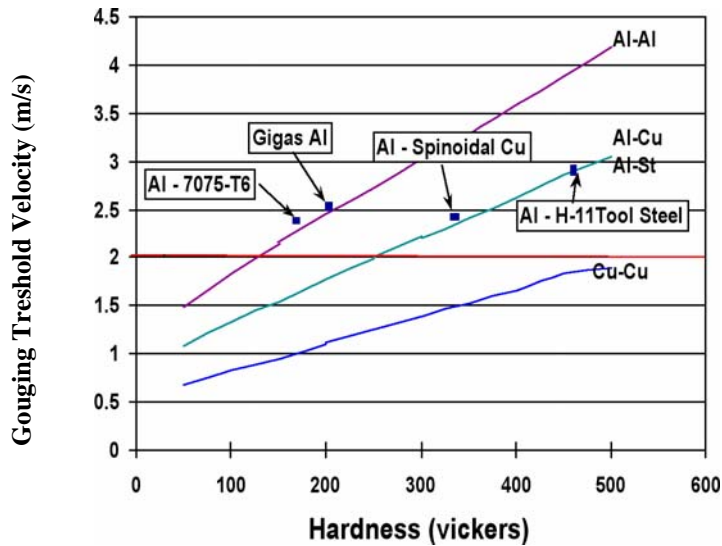
Figure 4.2.   Gouging Onset Velocity vs. Material Hardness

1.   Laser Peening

By using a ball-peen hammer, one can pound a piece of metal into shape, increase the surface hardness, and strengthen it against fatigue failure. For the past 50 years, an industrialized equivalent has been "shot peening", in which metal or ceramic beads pneumatically bombard a metal surface. Any peening process provides compressive stress at or near the surface layer, thereby retarding catastrophic growth of dislocations. One possible method to increase the hardness of rail material, as suggested in this thesis, is by laser peening the portion of the rail surface that is in direct contact with the armature.

Laser peening, a technology developed at Lawrence Livermore National Laboratory (LLNL), is a material hardening process that uses high-powered lasers capable of producing incredibly strong and resilient pieces of metals. At LLNL, a high energy, 600-watt laser fires 20-nanosecond pulses of light at the surface of a metal coated with dark paint and a thin layer transparent material — usually water. The laser pulse passes through the water and is absorbed by the dark paint. The interaction of the laser and the paint creates a pressure shock wave that is contained by the layer of water. The shock wave generates about 150,000 psi of pressure that in turn creates a deep compressive stress layer directly beneath the focused pulse. That compressed layer adds strength to the metal and helps prevent cracks.

Figure 4.3 shows the results from laser peening a nickel-based alloy (alloy 22). As shown, the hardness increased by approximately 66% at the surface. In conventional peening, the compressive layer is only about 0.25 millimeters deep. However, with laser peening, the shock wave from the laser pulse drives in a residual compressive stress about 1 to 2 millimeters deep into metals. One possible advantage of laser peening is that the increased hardness at greater depths may help prevent the formation of gouges where the crack originates at depths between 0.25 and 2 millimeters or greater.
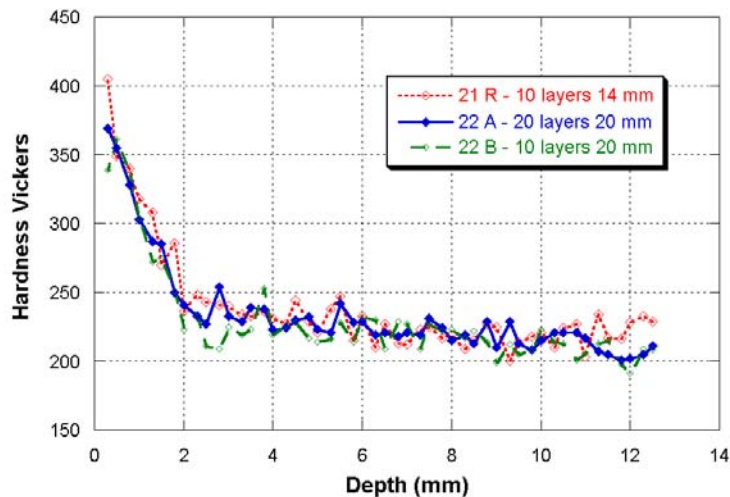

Figure 4.3.   Hardness vs. Depth for Alloy 22

Currently, the Institute of Advanced Technologies (IAT) at the University of Texas at Austin, in conjunction with LLNL, have begun a collaboration with the Naval Postgraduate School to test the hypothesis that laser peening may delay the onset velocity of gouging. Initial process and characterization tests have been conducted at the University of California at Davis (UC Davis) on laser peened Glidcop aluminum rails. Because the initial results indicated that the hardness of laser peened Glidcop is roughly equal to other peening process, a copper-tungsten alloy has been chosen for subsequent experiments. If initial results are successful, treated rails will be used in the IAT 40 mm bore railgun launcher to evaluate the extent to which gouging velocity is delayed.

Specifically, projectiles will be launched with one rail treated with laser peening while the other rail, containing the same material, will be untreated and will function as the control.

Thorough experimentation is needed to adequately evaluate the laser-peening hypothesis. However, using previously collected data, rough calculations can be made to estimate the possible benefits of laser peening railgun rails. As evidenced in figure 4.3, laser-peened metals can experience an increase of surface hardness of approximately 66%. Such an increase should significantly delay the gouging onset velocity. For example, a 66% increase in hardness for gigas aluminum, a metal currently being considered for railgun rails, would result in a hardness transition from 210 mm^2/kg to approximately 350 mm^2/kg (see figure 4.2). This hardness increase may result in a 0.7 km/s delay in the onset velocity of gouging. With a 15 kg projectile, the increase in projectile velocity would result in an additional 30 MJ of kinetic muzzle energy.

Several other benefits to laser peening rails exist as well. Due to the increased hardness of laser-peened materials, it is quite possible that metals that previously were not considered for use may be reconsidered. Some of the metals reintroduced for consideration may have favorable conductivity properties relative to intrinsically harder materials. Laser peening is relatively inexpensive. It can be used in conjunction with other techniques to reduce the gouging onset velocity. Peening may also increase the effectiveness of rail claddings and/or the armature by reducing long-term erosion.

B.   TRANSITION TO ARCING

Transition to arcing occurs when the sliding electric contact between the rail and armature changes from a low voltage, liquid film interface to a high voltage, plasma arc interface. Arcing is undesirable for several reasons. As Figure 4.4 (a) shows, it can cause rail and insulator erosion. Severe arcing can also destabilize the launch package as shown in Figure 4.4 (b) by causing the catastrophic failure of the armature material. However, transition does not appreciably reduce the efficiency of the launcher on a given shot.

<div align="center">
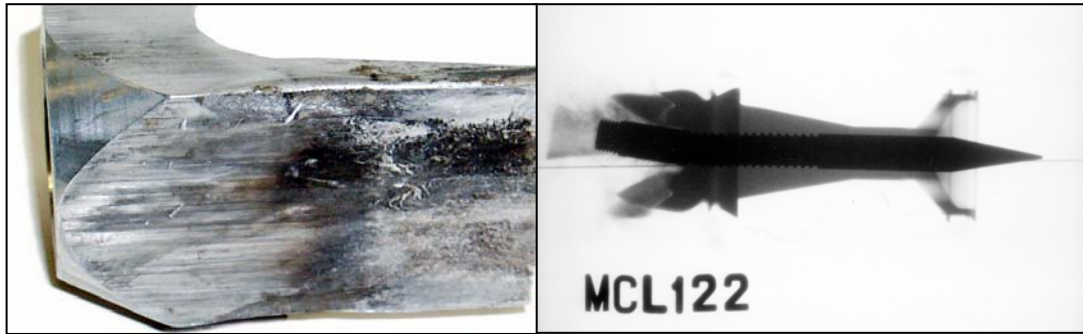
(a)   **(b)**

Figure 4.4.   Effects of Arcing: a) Surface Damage to Armature Resulting From High-voltage Arcing, b) Launch Package Resulting From Armature Arcing [Stefani, IAT]

</div>

Numerous mechanisms for armature transition have been proposed over the last two decades; however, neither experimental nor numerical evaluations have been able to validate any single mechanism as the primary cause of arcing. In a January 2003 paper, J.P. Barber et al [Ref. 4] suggested that several of the identified transition mechanisms contribute to arcing. Further, some or all of these causes may be dependant on the other known causes. Transition probably arises from a multiplicity of mechanisms, each of which must be controlled.

The "velocity skin current effect" is a chief cause of armature contact transition in railguns. This occurs when a thin layer of the armature contact surface evaporates in a high magnetic field region, which is induced by the mega-ampere level of current flowing between the surfaces. The evaporation leads to an increased voltage drop across the gap between the rail surface and armature and is followed by arc ignition when the magnetic field region collapses.

Another significant transition mechanism, sometimes called "negative I-dot transition", is associated with a rapid reduction in the driving current, as can be seen in Figure 4.5. As discussed in Chapter 3, if the current pulse is not properly conditioned, a steep drop-off in current magnitude often results. Typically, this mechanism occurs near

the end of the barrel. It only occurs in armatures that have survived the other arcing threats, and then only when a well-developed liquid film at the armature-rail interface is present.
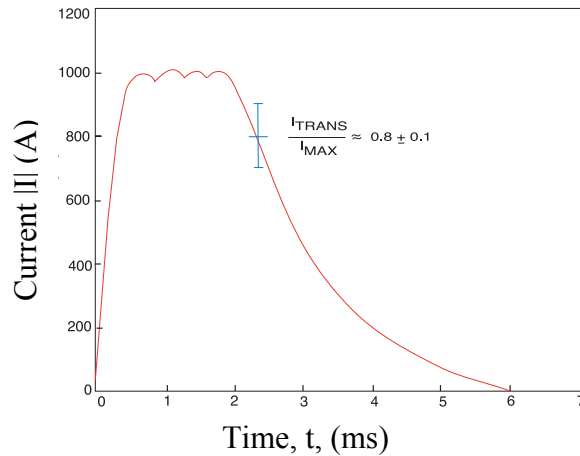

$$\frac{I_{TRANS}}{I_{MAX}} \approx 0.8 \pm 0.1$$

Figure 4.5.   Example of Current Slope Necessary to Initiate End-of-Launch Arcing

Stefani [Ref. 4] has postulated that this transition is caused by an electromechanical instability that disrupts the liquid film interface between the armature and the rail. As the magnetic field decreases in the launcher, a circulating current is produced on the surface of the armature facing the bore. The amplitude of this current is directly related to the rate at which the driving current is reduced. When the driving current is reduced rapidly enough, this circulating current can locally exceed the armature current density. This creates a negative net current on the trailing surface of the armature that leads to a local reversal of the Lorentz force. The "negative" force, generated by the axial component of the Lorentz force, pulls the liquid film out of the interface.

High-velocity surface wear is another mechanism that leads to transition. This occurs when mechanical shearing or viscous heating forces at the rail-armature interface cause material from the entire contact surface of the armature to be eroded. At high velocities, the thermal power generated by solid-on-solid friction swamps the ability of thermal conduction to carry the heat away from the interface. When a critical velocity is

44

reached, a layer of liquid armature material replaces the solid-on-solid interface. Any destabilization of the liquid interface then can cause arcing. If a significant portion of the film is ejected and gap between the armature and rail exist, arcing will occur. Often, the inward component of the force can lift the trailing edge of the armature off the rail, causing a destabilization of the liquid film, thus producing arcing. Although the theoretical proof of this mechanism is poorly developed, it has been observed in a large number of reproducible experiments.

THIS PAGE INTENTIONALLY LEFT BLANK

V.   CONCLUSION

The advent of the all-electric ship has proven to be a catalyst for the development of electric weapons for naval applications. Two examples of such weapons are the electromagnetic railgun and the free electron laser. Though considerable scientific and financial investment is necessary, if design challenges are overcome, these systems could transform the face of naval warfare. No known scientific reason exists that would prevent these systems from scaling to the level that the Navy has deemed necessary.

An overview of the free electron laser theory was presented along with a proposed design for a short-Rayleigh-length FEL. Simulations studied how optical characteristics are affected by variations in the electron beam focal point along the length of the undulator. Findings show that in weak fields optical gain remains above threshold output coupling regardless of such variations. In strong fields, moderate variations in the electron beam focal point will not significantly affect optical extraction. It is also concluded that mirror survivability is largely unaffected by electron beam focal point variations.

Electromagnetic railgun theory was discussed in detail. Designed from first principles, a numerical railgun model is presented that simulates the railgun circuit, joule heating, and the performance of the projectile. For the parameters chosen, the effects of varying rail materials, barrel geometries, and projectile characteristics were discussed.

Laser peening of railgun rails was proposed as a possible method to increase the onset velocity of gouging. If successful, this technique would also apply to rocket sled tracks and light-gas (e.g. hydrogen) guns. Status of testing was discussed.

THIS PAGE INTENTIONALLY LEFT BLANK

LIST OF REFERENCES

1.   W.B. Colson, Laser Handbook, Vol. 6., Chap. 5, Eds, W. B. Colson, C. Pellegrini and A. Renieri, North Holland, Amsterdam (1990).

2.   W. B. Colson, *Short Wavelength Free Electron Lasers in 2000*, http://www.physics.nps.nav.mil/table1.pdf. last accessed June 2004

3.   McNabb, I., "Navy EM Launcher", PPT presented at the Naval Postgraduate School, Monterey, Califonia. 15 June 2004.

4.   Barber, J.P., et al, A Survey of Armature Transition Mechanisms, IEEE Tranactions on Magnetics, Vol. 39, No. 1, January 2003.

THIS PAGE INTENTIONALLY LEFT BLANK

INITIAL DISTRIBUTION LIST

1.   Defense Technical Information Center
      Ft. Belvoir, Virginia

2.   Dudley Knox Library
      Naval Postgraduate School
      Monterey, California

3.   Prof. William B. Colson
      Naval Postgraduate School
      Monterey, California

4.   Prof. Robert L. Armstead
      Naval Postgraduate School
      Monterey, California

5.   Prof. Joseph Blau
      Naval Postgraduate School
      Monterey, California

6.   Prof. Peter Crooker
      Naval Postgraduate School
      Monterey, California

7.   Prof. James H. Luscombe
      Naval Postgraduate School
      Monterey, California

8.   CAPT Roger McGinnis, USN
      Naval Sea Systems Command
      CODE SEA 53R
      Washington Navy Yard, DC

9.   Fred Dylla
      TJNAF
      Newport News, Virginia